metals

MDPI

Article

Microstructural Characterization of Martensitic Stainless Steel Blades Manufactured by Directed Energy Deposition (DED)

Caroline Cristine de Andrade Ferreira [1], Rafael Humberto Mota de Siqueira [2], Johan Grass Nuñez [3], Fábio Edson Mariani [3], Reginaldo Teixeira Coelho [3], Daolun Chen [4] and Milton Sérgio Fernandes de Lima [1,2,*]

[1] Graduate Program in Space Sciences and Technologies, Technological Institute of Aeronautics, Praca Eduardo Gomes 50, Sao Jose dos Campos 12228-901, SP, Brazil; carolinecaferreira@gmail.com or carolineferreira@ita.br
[2] Photonics Division, Institute for Advanced Studies, Trevo Amarante 1, Sao Jose dos Campos 12228-001, SP, Brazil; rhmotasiqueira@gmail.com
[3] Laboratory for Advanced Process and Sustainability, Department of Production Engineering, School of Engineering at Sao Carlos, University of Sao Paulo, Sao Carlos 13566-590, SP, Brazil; jsgrassn@usp.br (J.G.N.); fabio.mariani@ccm-ita.org.br (F.E.M.); rtcoelho@sc.usp.br (R.T.C.)
[4] Department of Mechanical, Industrial and Mechatronics Engineering, Toronto Metropolitan University, Toronto, ON M5B 2K3, Canada
* Correspondence: milton.lima@gp.ita.br; Tel.: +55-12-3947-5464

Abstract: This study explores the feasibility of manufacturing martensitic stainless steel turbine blades via a directed energy deposition (DED) process using a powder precursor. Five different blade geometries were fabricated using AISI 431 L martensitic stainless steel deposited onto an AISI 304 L austenitic stainless steel substrate. The produced components were characterized in terms of microstructure, surface roughness, porosity, hardness, and residual stresses in both the as-processed condition and after heat treatment at 260 and 593 °C. Optical and scanning electron microscopy (SEM) analyses revealed a predominantly martensitic microstructure with well-defined grain boundaries. Heat treatment influenced the phase distribution and grain size, but did not have a significant impact on the surface roughness or modulus of elasticity. Tomographic assessments confirmed the absence of aligned or coalesced pores, which are critical sites for crack initiation. Residual stress analysis indicated the presence of compressive stresses in all blade geometries, which were effectively relieved by heat treatment. In addition, salt spray corrosion tests demonstrated that the corrosion resistance of the manufactured blades was similar to that of the base material. These findings suggest that DED is a viable technique for producing and repairing turbine blades, providing structural integrity and mechanical properties suitable for high-performance applications.

Keywords: directed energy deposition; martensitic stainless steel; microstructural characterization; turbine blades

check for updates

Academic Editor: Umberto Prisco

Received: 25 March 2025
Revised: 3 May 2025
Accepted: 13 May 2025
Published: 29 May 2025

Citation: Ferreira, C.C.d.A.; Siqueira, R.H.M.d.; Nuñez, J.G.; Mariani, F.E.; Coelho, R.T.; Chen, D.; Lima, M.S.F.d. Microstructural Characterization of Martensitic Stainless Steel Blades Manufactured by Directed Energy Deposition (DED). *Metals* **2025**, *15*, 612. https://doi.org/10.3390/met15060612

1. Introduction

Additive manufacturing (AM) has disrupted the global paradigm of product development and manufacturing. Owing to the agility, precision, and economic efficiency of customizing parts compared to other manufacturing methods, there is immense interest in their applications in the aerospace, energy, biomedical, automotive, and metalworking industries [1]. AM provides controlled addition of material in layers to a given substrate based on the design and selection of materials in the development of a component through a 3D computational geometric model [2]. Efficient repair methods are extremely important for introducing fast, environmentally friendly, and low-cost reconstruction techniques that can extend the useful life of a tool without compromising its dimensional characteristics [3].

In recent years, one of the applications that has received great importance and interest in the industry is the use of lasers to repair components with high added value [4]. Turbine blades are a classic example of components that are sensitive to operating conditions, in which high thermal cycles and the impact of particulates limit their lifespan. Turbine blades are the most important components of a gas turbine. Generally, they are made of alloys resistant to high temperatures, such as Fe-based and Ni-based alloys, with a higher specific cost, that is, high cost and low weight [5]. These components are made of high-value materials (Ni, Ti, Zr, etc.) because they are subjected to a corrosive environment, the high velocity and temperature of the combustion gas, large centrifugal forces, fatigue, and thermal shock, and are expected to withstand more than 30,000 h of operation if applied for energy generation [6].

Oxidation at high temperatures and other reactions in corrosive environments are important factors in the development of turbine blades. Thus, the metals used in turbines are based on transition metals, such as iron, nickel, and cobalt, and the oxidation resistance can be increased by the addition of Cr, Al, and Si to form external oxides in the material. However, they are also highly reactive at high temperatures. As iron alloys and refractory materials have excellent mechanical strength but low corrosion resistance, it is necessary to create a protective coating for these components to increase their useful life [6].

Stainless steels, which are resistant to corrosion and oxidation, are iron-based alloys containing Cr as the main alloying element with a minimum concentration of 10.5% by weight. Alloy elements such as nickel, molybdenum, manganese, copper, titanium, niobium, and aluminum, among others, are added to stainless steels in order to improve their properties [7].

Stainless steels are classified into five main groups representing three distinct types of metallurgical structures: martensitic, austenitic, ferritic, precipitation-hardened, and duplex stainless steels [7]. Martensitic stainless steels, series 400, are characterized by their ability to harden through heat treatment, which consists of heating until complete austenitization, followed by cooling in ambient air, thus transforming into a martensitic structure. It has a chromium concentration between 11 and 18% and a carbon weight percentage between 0.10 and 1.2%. These steels are used in applications that require moderate corrosion resistance, relatively high mechanical strength, and good fatigue resistance.

The growth of stainless steel blades through directed energy deposition (DED) has been reported in the literature [8,9]. Compared to Inconel blades, stainless steel blades have good mechanical properties and lower prices, and are usually chosen for gas turbine blades [10]. Zu et al. [8,9] performed gas turbine blade growth using 316 L austenitic stainless steel powder via DED. These authors used a Nd/YAG laser with powers ranging between 250 and 560 W, a scanning rate between 5 and 12 mm/s, and a powder flow between 4.2 and 12 g/min. Consequently, they obtained blades with directional growth microstructures, interdendritic segregation, and surface roughness between 10 and 26 μm (Ra). The authors reported a certain difficulty in the spatial resolution of the blades, particularly at the corners, where the deposition speed needed to be reduced.

Saboori et al. [3] documented repair using DED in a review article, including repair work on turbine blades using DED. The authors summarized the problems intrinsic to this repair, including the issue of the directionality of the microstructures formed, and how this affects the behavior of the repaired reed at high temperatures. To the best of our knowledge, there has been no systematic study on the growth of AISI 431 L martensitic steel turbine blades on AISI 304 austenitic steel substrates with different geometries.

The objective of the present study was to determine the feasibility of manufacturing five different types of turbine blades composed of AISI 431 L martensitic steel on an AISI 304 austenitic steel substrate by directed energy deposition (DED), and to characterize the components for critical applications in gas turbines.

In this study, the possibility of growing AISI 431 L (martensitic) steel blades on AISI 304 L (austenitic) steel substrates is verified. The motivation for this dissimilar growth lies in the improvement of the mechanical properties of the blades, which are subject to erosion, cavitation, and wear, while maintaining the shaft volume of a tougher material at turbine operating temperatures. Özdemir [11] carried out a similar study of austenitic/martensitic stainless steel where the joint between parts was made by friction stir welding, showing the gain in terms of tensile strength at rupture. In addition to aiming for blades that are more resistant to wear mechanisms, in a practical way, it is possible to use old AISI 304 L steel rotors and grow new AISI 431 L blades to extend their service life [12].

Additionally, because of the aerodynamic forces acting on a blade and the fact that these forces vary along its entire length, a variable distribution of forces and stresses is generated throughout the blade. Therefore, the use of different aerodynamic profiles along the blade is required to optimize the structural performance and aerodynamic efficiency.

2. Materials and Methods

2.1. Raw Materials

AISI 304 L austenitic stainless steel with a thickness of 20 mm was used as a substrate (Acesita Co., Campinas, Brazil). Compatibility of the chemical compositions was considered for the deposition of AISI 431 L stainless steel onto AISI 304 L. The feedstock material consisted of gas-atomized AISI 431 L stainless steel powder with a particle size range of 53–150 µm and a spherical shape (Högänas Co., Mogi das Cruzes, Brazil). Table 1 lists the chemical compositions of the substrate and powder used according to the furnishers.

Table 1. The chemical compositions of the substrate and the powder (wt.%).

Type	C	S	Ni	Cr	Si	Fe
Substrate	0.07	0.03	9.5	18.5	0.75	~Balance
Powder	0.150–0.250	0.030	1.25–2.50	15.00–17.00	1.00	~Balance

2.2. DED Processing

The deposition of powder on the substrate was performed using the direct energy deposition technique with a BeAM Modulo 250 equipment (AddUp, Cébazat, France) equipped with five independent axes, a Siemens 840D controller (Siemens, Munich, Germany), and a working volume of 0.4 m × 0.25 m × 0.3 m. The optical power of the fiber laser was 1 kW (IPG Photonics) and was coupled to a MacroClad 10Vx (AddUp, Cébazat, France) deposition head connected to a powder distributor.

To construct the process chart, a single deposition layer was created by varying the laser power, scan speed, and powder flow rate. Five laser power values (300, 350, 400, 500, and 550 W), three process speeds (1800, 2000, and 2200 mm/min), and two powder flows (4.70 and 8.42 g/min) were utilized, resulting in thirty-six combinations of process parameters. After conducting the thirty-six tracks, the six best conditions (Table 2), considering the layer's adherence to the substrate, track regularity, and whether surface oxidation occurred, were reproduced. The final condition was chosen from the reproduced data using the same criteria (laser power: 450 W; process speed: 2000 mm·min^{-1}, and 8.42 g·min^{-1}), giving a layer thickness of 0.25 mm.

Table 2. Best deposition conditions.

Laser Power	Process Speed	Powder Flow
400 W	1800 mm·min^{-1}	4.70 g·min^{-1}
400 W	2000 mm·min^{-1}	4.70 g·min^{-1}
450 W	2000 mm·min^{-1}	4.70 g·min^{-1}
450 W	1800 mm·min^{-1}	8.42 g·min^{-1}
450 W *	2000 mm·min^{-1} *	8.42 g·min^{-1} *
450 W	2200 mm·min^{-1}	8.42 g·min^{-1}

* Chosen parameters.

2.3. Heat Treating

Heat treatment was conducted at two different temperatures, 260 °C and 593 °C, for 3 h, followed by air-cooling. These specific temperatures were selected using the CES Edupack version 2009 material selection software, tailored for tempering this class of steel. The furnace was preheated and calibrated prior to the initial heat treatment. Upon reaching 260 °C, the samples were placed inside a furnace on a refractory brick and maintained for 3 h. Subsequently, the samples were extracted from the furnace and placed on a bench for 3 min to cool air. After completing the first heat treatment, a second cycle was initiated at 593 °C, with the samples air-cooled for 5 min post-treatment to reduce hardness.

2.4. Analytical Methods

Microstructural analyses using optical microscopy (OM) were performed with a ZEISS microscope (Axion Image A2m, Zeiss AG, Oberkochen, Germany). Scanning electron microscopy (SEM) and energy-dispersive X-ray spectroscopy (EDS) were performed using a JEOL JSM-6380LV microscope (JEOL, Akishima, Japan) equipped with an Oxford energy-dispersive spectrometer (Oxford Instruments PLC, Oxfordshire, UK). Backscatter electron diffraction was performed using an Oxford AZtecHKL integrated system assembled with NordlysMax2 and AZtecSynergy (Oxford Instruments PLC, Oxfordshire, UK) equipped with a large-area analytical detector.

For microstructural analysis using OM, SEM, and EDS, the samples had to be prepared previously, requiring cutting, mounting, grinding, polishing, and etching. The samples were cut transversely to the growth of the layers using wire electric discharge machining (EDM) and subsequently embedded in epoxy resin. The embedded samples were ground using silicon carbide wet sandpapers with particle sizes of 240, 320, 400, 600, 800, 1000, and 1200 meshes. Polishing was performed using diamond colloidal solutions of 6, 3, and 1 µm and finished with alumina suspensions of 0.3 and 0.05 µm. The samples were electrolytically etched with 10% oxalic acid (aqueous solution) at a voltage of 6 V for 30 s according to ASTM E407-99 [13].

X-ray diffraction (XRD) analyses were performed using a Rigaku instrument (model Utima IV) with Cukα radiation (λ = 1.54178 Å), a current of 30 mA, and a voltage of 40 kV. X-ray diffractograms were obtained with 2θ ranging from 30 to 90°. Phase analyses were performed using the Crystallographic Open Database, version 2025.

The residual stress was estimated via X-ray diffraction (XRD) using a Rigaku Ultima IV diffractometer (Rigaku Co., Tokyo, Japan). A copper anode with a radiation wavelength of 1.54051 Å and a voltage and current of 40 kV and 30 mA, respectively, was used. The method used to estimate the residual stress was a lateral shift with an angle ψ between 0° and 30°. Each diffraction peak was treated analytically to remove background noise, correct for Lorentz polarization, deconvolute the kα 1/kα 2 contribution, and correlate the data with a Gaussian distribution to determine the position of the maximum diffracted intensity. A linear regression between the peak angle and the value of sin ψ 2 determined the residual stress. Each condition was analyzed three times.

Nanoindentation tests were performed to create a hardness map in the interface region between the substrate and the deposited layers using Wrexham NanoTest-600 equipment, with the capacity to operate in two modules (the maximum load of the first module was 40 mN and that of the second was 500 mN). The load used was 5 mN, and the loading and unloading times were 30 and 90 s, respectively, per indentation. Two matrices were created with two lines of forty-two indentations.

The ultramicrohardness test was performed using a Fischer Instruments (Fischercope H100, Fisher Group, Achern-Fautenbach, Germany). Two loads were used: 50 mN and 100 mN. For the 50 mN load, the indentation spacing was 0.1 mm and for the 100 mN load, the spacing was 0.2 mm. For the 100 and 50 mN loads, 36 and 20 indentations were made, respectively, starting from the substrate and ending at the deposition. By using the ultramicrohardness results, it was possible to obtain the modulus of elasticity (E).

The tomography test was performed using Bruker X-ray computed microtomography (micro-CT) model SkyScan 1275. An acceleration voltage of 100 kV and beam current of 100 µA were applied using a 1 mm thick copper filter in the step-and-shoot mode. The pixel size was set to 7 µm × 7 µm and the mode was random. In total, 2248 projection images were acquired in 360° angular steps, with an average of three frames per step, using an exposure time of 145 ms. Micro-CT images were reconstructed using a dedicated software from the manufacturer. A sample measuring 15.6 mm long, 5.0 mm high, and 1.0 mm thick sample was used for the analysis.

Salt spray corrosion tests were performed in accordance with ASTM D1654 [14]. The test was carried out in the climatic test laboratory for a period of 1080 h, for 45 days, in a Weiss Salt Spray Chamber (model SC1000, Weiss Technik AG, Hessen, Germany).

3. Results

3.1. Fabrication of the Blades

In Boulila [15], the complexity of the blades required precise knowledge and control of the manufacturing conditions, as deviations in finishing can compromise their performance at high temperatures. Traditionally, turbine blades have been manufactured through casting and machining. In casting, liquid metal is poured into molds, and machining uses a CAD design in machining centers. Cast blades require additional machining for dimensional adjustments and surface finishing [16].

In this study, AISI 304 stainless steel with an austenitic microstructure was used as the substrate, and AISI 431 L stainless steel powder was used, with particle sizes ranging from 53 to 150 µm, approximately spherical in shape with a martensitic microstructure. This material is widely used in various applications owing to its excellent properties such as corrosion resistance. It contains chromium, which forms a passive chromium oxide layer on the surface of the material, thereby protecting it against corrosion. This makes it suitable for use in humid, chemical, and saline environments. It is highly durable and can withstand adverse conditions such as exposure to extreme temperatures, thermal shock, and mechanical wear [17].

Considering the relationship between the laser power and scanning speed, this relationship has the opposite impact on the properties of the deposited layer [18], which is manifested through the energy density of the laser beam (E) [19]. The best set of parameters was a process speed of 2000 mm/min, power of 450 W, and powder flow of 8.47 g/min. With the process parameters already chosen, five blade geometries were grown: Clark, Later, Laminar, Arc, and Supersonic, as shown in Figure 1. These five geometries were selected because of their widespread use in turbine blade construction and aircraft wings [20].

All blades were grown with approximately 43 layers, with each layer having an average thickness of 0.25 mm and a blade height of 10 mm, and the length of each blade was 100 mm.

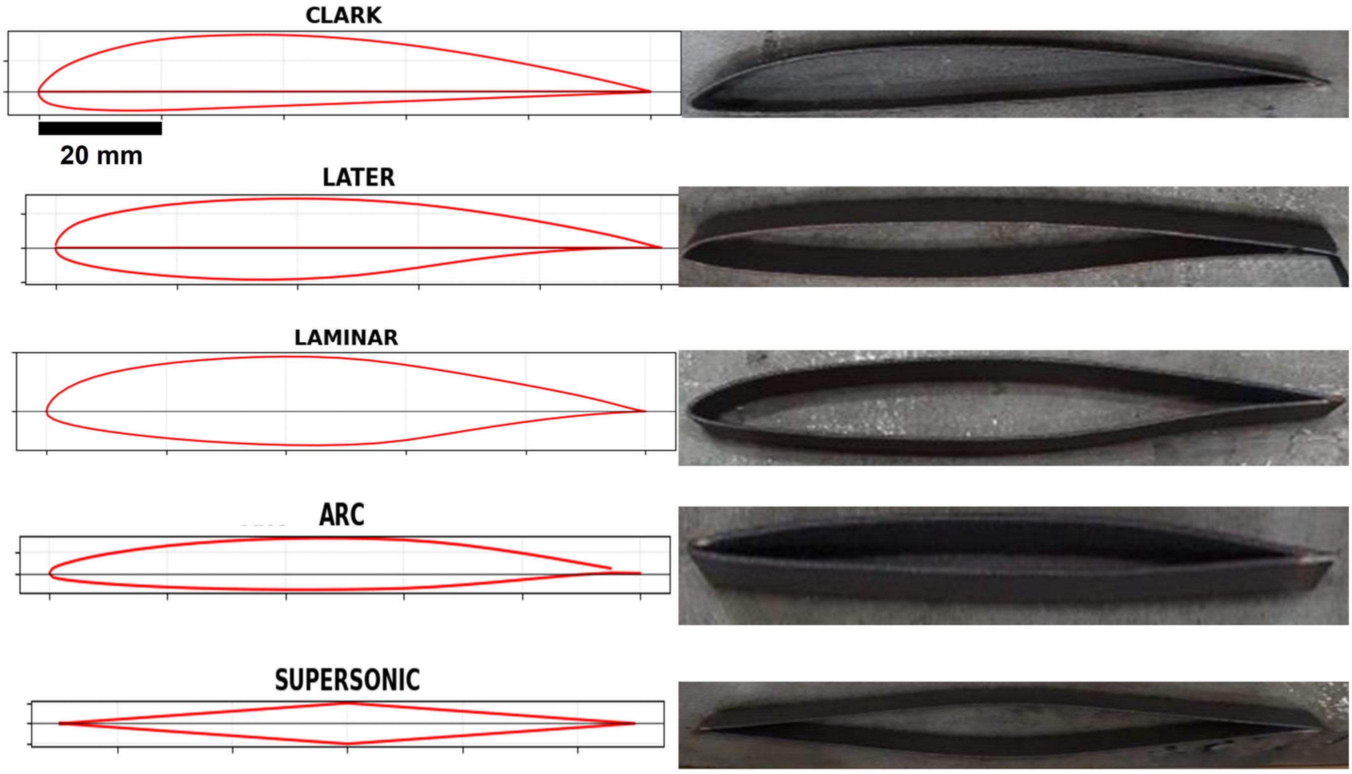

Figure 1. Top-view representation of each blade (**left**) compared to the real ones (**right**). A scale bar is applied to all images.

3.2. Microstructure

In Figure 2, the middle longitudinal and cross-sections of the deposition performed by DED are presented for the as-processed sample. The upwards arrows indicate the growth direction. In Figure 2a,b, bright and dark regions can be observed, corresponding to the interlayer regions and the deposited layer, respectively. The color difference in these regions is associated with variations in the reactivity to the chemical etching reagent, as remelting occurs between the layers owing to the deposition of the upper layer. The average layer width was measured using NIH ImageJ software version 17.1, resulting in a value of 24 ± 4 µm. The arrow in Figure 2a indicates a pore.

In Figure 3, the cross-sections of the samples in the middle are presented: (a) as-processed and after heat treatment at (b) 260 and (c) 593 °C. The macrographs show that the as-processed sample and the sample that was heat-treated at 260 °C exhibited morphologies similar to those visible deposition layers. In contrast, the sample heat treated at 593 °C macroscopically no longer displayed deposition layer marks, as a result of homogenization of the intercellular microsegregation.

In the images shown in Figure 4, the microstructures of the central region of the deposits are presented using optical microscopy: (a) as-processed and after heat treatment at (b) 260 °C and (c) 593 °C. A microstructure image of the as-processed sample is presented in Figure 4a, where a solidification structure composed of dendrites and well-defined grain boundaries can be observed [20–22]. The sample subjected to heat treatment at 260 °C, as shown in Figure 4b, did not exhibit dendrites due to the short-range segregation [23].

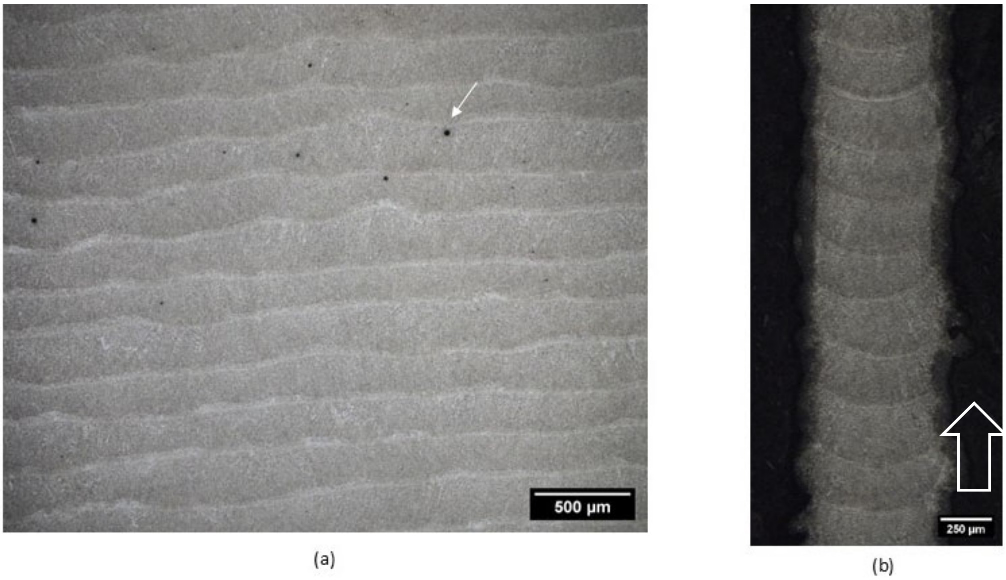

(a)

(b)

Figure 2. Macrographs of the longitudinal (**a**) and cross-sections (**b**) of the as-processed sample. The growth direction was upward as given by the arrows.

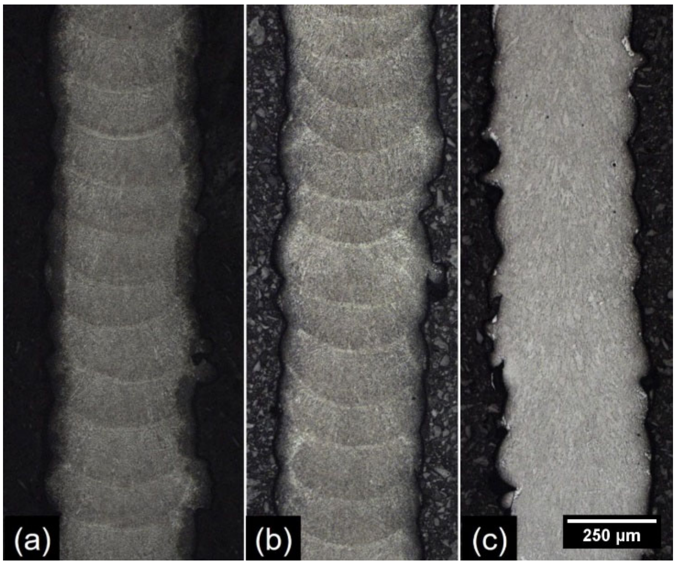

Figure 3. Macrographs of the cross-sections of the samples: (**a**) as-processed and after heat treatment at (**b**) 260 °C and (**c**) 593 °C.

As shown in Figure 4c, when the sample was subjected to heat treatment at 593 °C, its microstructure was similar to that of the sample treated at 260 °C. Considering that images in Figure 4b,c have the same magnification, a decrease in grain size was observed. A temperature of 593 °C and treatment time promoted the recrystallization process due to long-range segregation [24,25].

The metabisulfite reagent does not differentiate the phases present in the microstructure [26]; however, it is known that the microstructure consists of martensite, ferrite, and carbides [27,28]. Because of the reagent's inability to distinguish the phases, it was not possible to quantify their concentrations or determine whether the heat treatment altered the phase proportions.

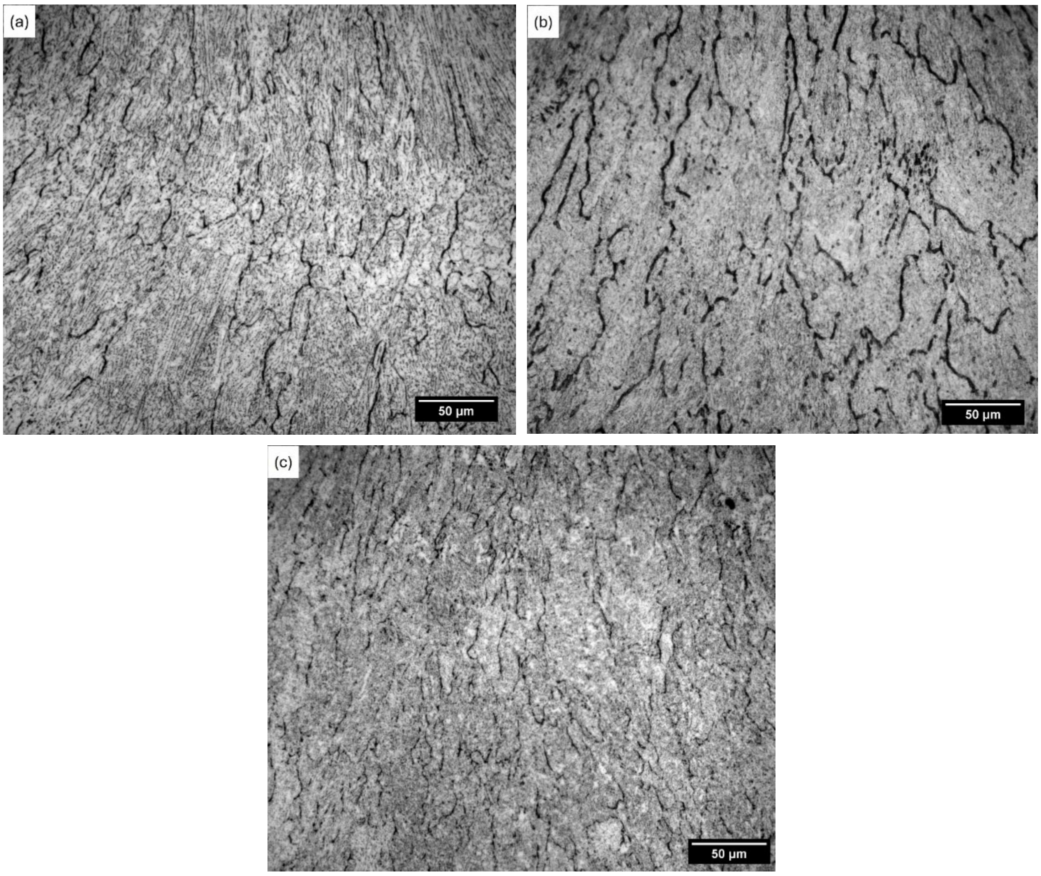

Figure 4. Optical microscopy images of the central region of the deposition: (**a**) as-processed and after heat treatment at (**b**) 260 and (**c**) 593 °C.

The images in Figure 4 show well-defined grain boundaries in both the as-processed and heat-treated samples. During solidification, segregation occurs at the grain boundaries, and because of the high solute concentration in this region, the likelihood of precipitate formation, such as carbides, is high [24,25,29]. By visually examining the images without quantitative analysis, it was not possible to confirm whether the sample treated at 260 °C (Figure 4b) exhibited a decrease in solute concentration at the grain boundaries. Heat treatment at 593 °C promoted recrystallization; however, owing to the high temperature and treatment time, segregation at the grain boundaries occurred again. The concentration of precipitates at the grain boundaries can be detrimental to mechanical properties, because cracks may nucleate in this region and propagate transgranularly [30].

Figure 5 presents the microstructures of the central region of the depositions obtained via scanning electron microscopy: (a) as-processed and after heat treatment at (b) 260 °C and (c) 593 °C. The images in Figure 5 show a predominantly martensitic microstructure, which is the main phase of AISI 431 L steel [23,27], indicating that the heat treatment did not affect the formation of the martensitic phase.

Figure 6 presents a scanning electron microscopy image of the interface between the first deposited layer and AISI 304 steel substrate of the sample treated at 593 °C. Well-defined grain boundaries were observed in the substrate, indicating that the temperature and treatment time caused segregation at the grain boundaries, thereby promoting substrate sensitization [31,32].

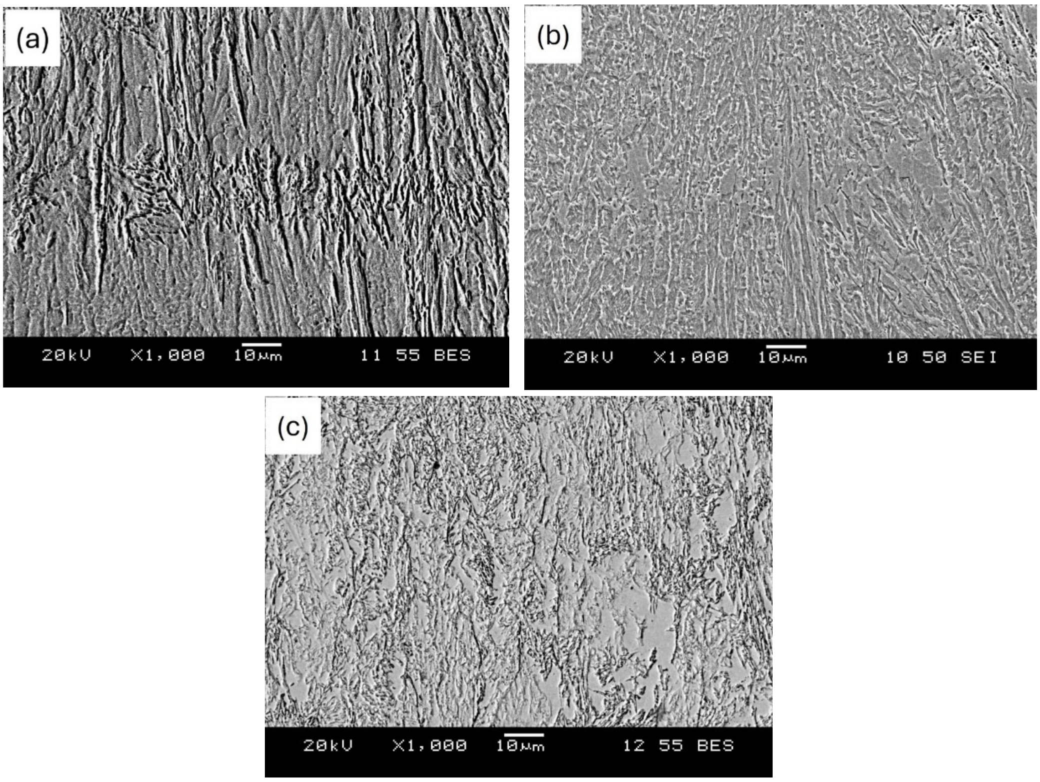

Figure 5. Scanning electron microscopy images of the central region of the deposition: (**a**) as-processed and after heat treatment at (**b**) 260 °C and (**c**) 593 °C.

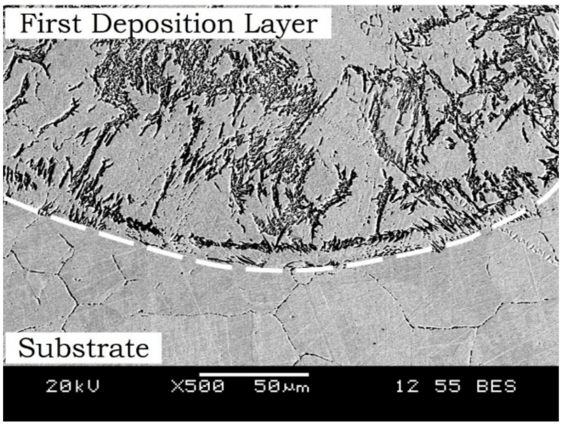

Figure 6. Scanning electron microscopy image of the interface between the first deposited layer and the AISI 304 steel substrate of the sample treated at 593 °C.

3.3. Crystallographic Orientations

As already known in the literature, additive manufacturing implies crystallographic features such as directional growth, and is sometimes similar to ordinary casting [33]. Understanding the crystallographic orientation of each phase is of utmost importance in determining the macroscopic properties of the AISI 431 L steel blades in this study.

Independent of the fabrication procedure, that is, the blade shape, the EBSD patterns of different regions of interest (substrate, interface, and deposit) were similar. Therefore, the crystallographic features were considered identical.

Figure 7a presents a representative light optical micrograph of a single-track cross-section, indicating the regions of interest. As expected, the austenitic substrate exhibited large FCC grains without any particular crystallographic orientation, except for twinned intragranular slats, as shown in Figure 7b. The image in Figure 7c shows the interface region (Figure 7a), where both FCC and BCC grains were indexed. The indexed BCC crystals in the martensitic region indicated that tetragonal distortion of the cell was not verified. This indicates low-carbon martensite, which was indexed as BCC. The deposited material is characterized by a much finer BCC grain compared to the substrate, and expitaxy could be verified as some substrate FCC grains entered the fusion zone. The line of deposited BCC crystals indicates dilution, which, together with epitaxial growth, reflects convenient metallurgical bonding. Figure 7d shows the IPF orientation map of the deposit region (indexing referenced in Figure 7e). The preferential growth direction of the BCC dendrites is not evident in the image in Figure 7d, as can be seen in the pole figures in Figure 7f. The pole figure in Figure 7f represents the untreated deposit under optimized conditions (Table 2). The absence of crystallographic orientations due to equiaxial grains ahead of the solidification front or because of the metallographic cross-section not being completely aligned to the thermal gradient has already been reported in the literature [33,34].

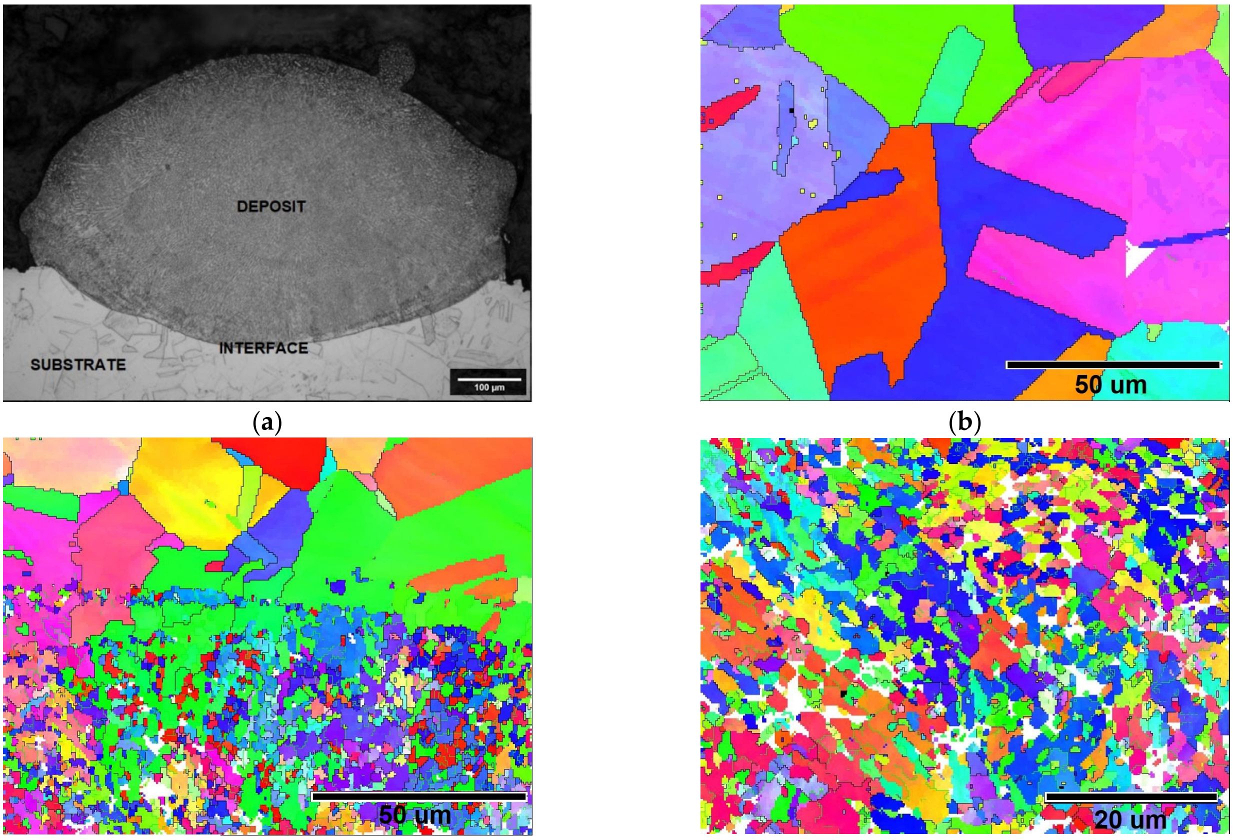

(**a**) (**b**)

(**c**) (**d**)

Figure 7. *Cont.*

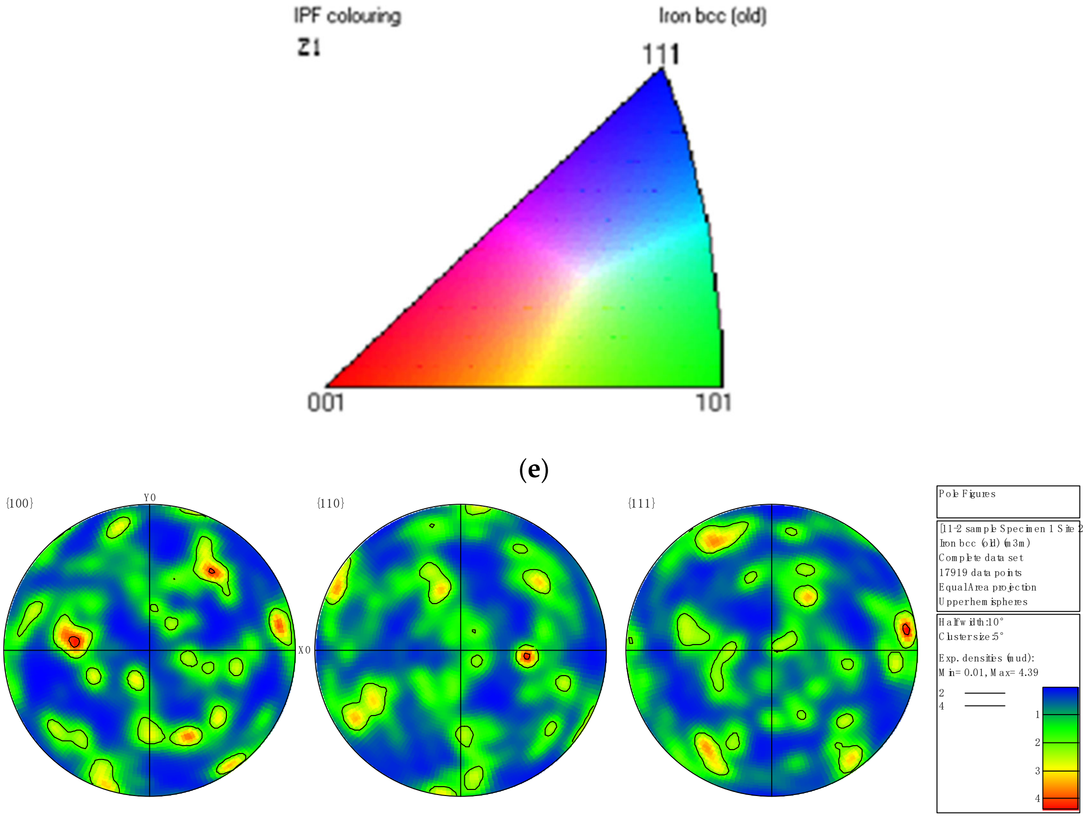

(**e**)

(**f**)

Figure 7. (**a**) Light optical micrography of a cross-section of a single line of deposition using 450 W laser power, 2 m/min speed, and a powder flux rate of 8.42 g/min. (**b**) EBSD-IPF orientation map of substrate. (**c**) EBSD-IPF orientation map near interface. (**d**) EBSD-IPF orientation map of the deposit (single line). (**e**) IPF color scale. (**f**) Pole figures of the deposits.

The EBSD analyses of the as-grown blades are shown in Figure 8. Figure 8a presents a general view of the IPF artificially colored EBSD orientation map of both FCC (substrate) and BCC (deposit). Unlike single-track analyses (Figure 7), there is a barely visible tendency of the dendrites around the "deposit" to growth obliquely to the observation plane. However, by observing many EBSD images, the grain growth direction in the deposit could not be determined. Figure 8b shows an extract of the same region of the image in Figure 8a, indicating the indexed FCC (green) and BCC (red) phases. As shown in Figure 8b, the dilution of the substrate/deposit is approximately 5 µm, as indicated by the red grains at the bottom of the image. The deposit was composed of a BCC phase with intergranular FCC, with an FCC content of approximately 10% (Figure 8b). The presence of small amounts of retained austenite in welded AISI 430 steels has been reported as a result of the reheating of the microstructure at approximately 1000 °C [35] or due to the microsegregation of austenite-stabilizing elements (C, Mn, etc.) in the interdendritic spaces [36,37]. In terms of morphology, the grains in the deposit had an average size of 2 µm and half of the grains were between 0.8 and 3 µm. The grain aspect ratio varied between 0.4 and 0.75, with a peak at 0.55, showing a tendency of alignment to the substrate heat sink. The pole figures of the packed planes are shown in Figure 8c. In the figure, the growth direction of the deposit is RD and the laser cladding scanning is TD. As can be seen, the preferential orientation of BCC crystals was not evident, similarly to that reported for the as-built AISI 316 L stringers [37].

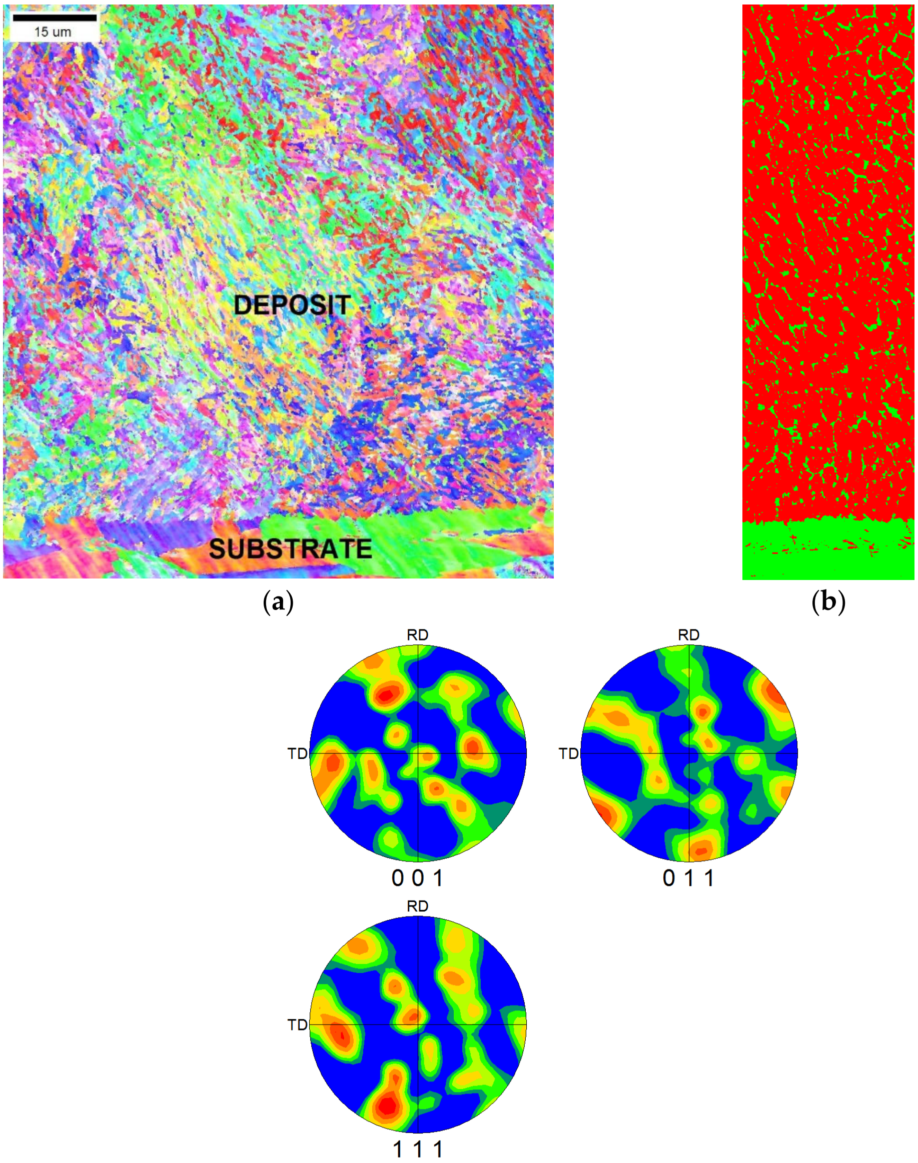

(**a**) (**b**)

(**c**)

Figure 8. (**a**) IPF orientation maps of the deposit and substrate. (**b**) Extract of the phase identification (phase map) in the middle of image (**a**), with FCC (green) and BCC (red) crystals. (**c**) Pole figures for different crystallographic directions.

As mentioned previously, the blades were subjected to two different heat-treatment temperatures: 260 °C and 593 °C. Figure 9 shows the related EBSD-IPF orientation maps at 260 °C (Figure 9a) and 593 °C (Figure 9b) and pole figures of the deposit indexing at 260 °C (Figure 9c) and 593 °C (Figure 9d). As verified for the untreated deposits (Figure 8), there was no definite crystallographic orientation after the heat treatment (Figure 9). The grain size increased after the heat treatment in both cases, and the phase fractions also changed. After heat treatment at 260 °C, the amount of FCC phase increased to 33% compared to approximately 10% of that of the untreated deposit. However, heat treatment at 593 °C reduced the FCC phase to approximately 4%, according to EBSD analyses.

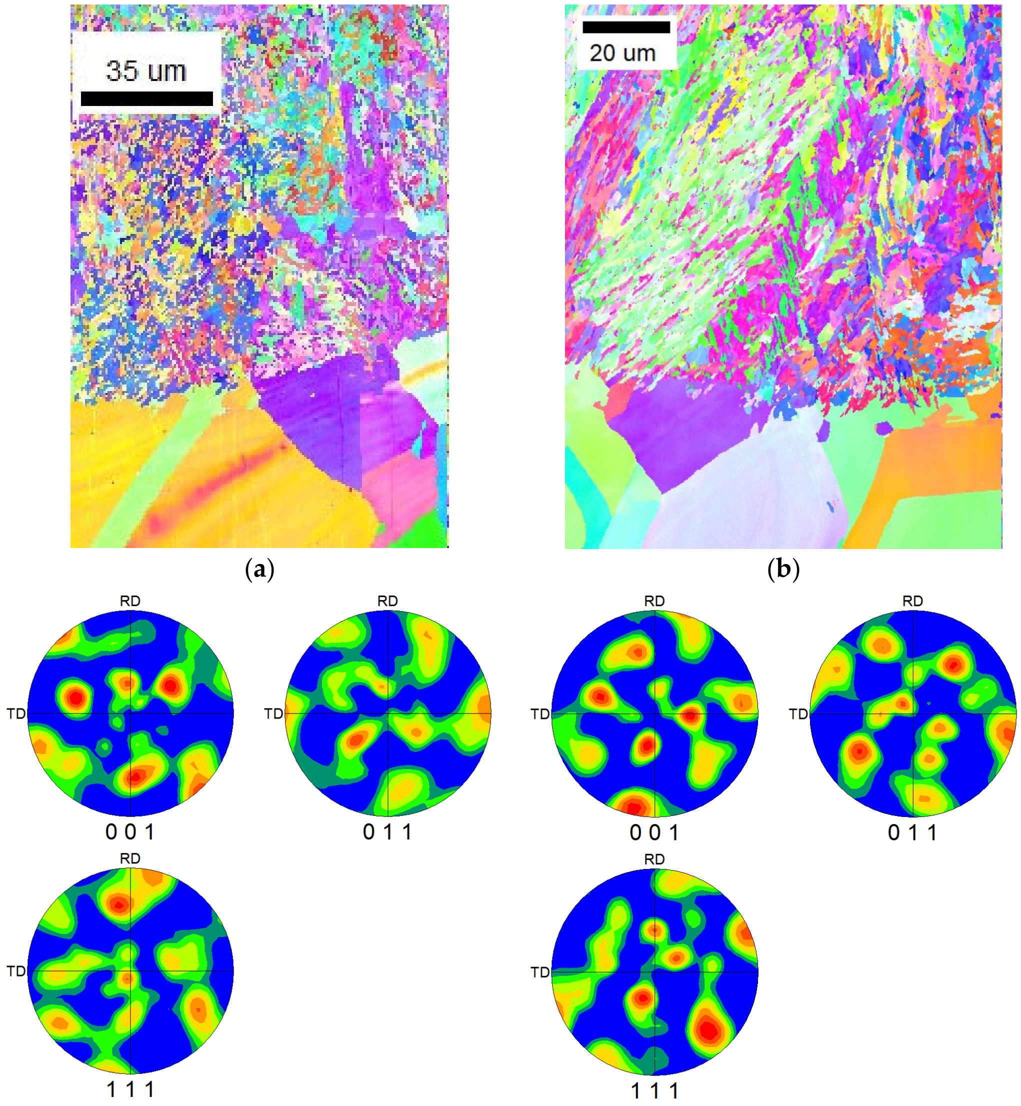

(**a**) (**b**)

(**c**) (**d**)

Figure 9. EBSD IPF orientation maps of samples heat-treated at (**a**) 260 °C and (**b**) 593 °C near the interface between the deposit and substrate. Pole figures of the deposits for (**c**) 260 °C and (**d**) 593 °C samples.

3.4. Tomograph

In Figure 10, tomographic images of the as-processed sample are presented, showing the front, top, side, and isometric views. Considering an equipment resolution of 5.0 µm, no pores were observed in the sample volume. In Figure 2a, pores are visible, as indicated by an arrow in the image, and measurements performed using NIH ImageJ software revealed that the average pore diameter is 1.8 ± 0.7 µm, which is 64% smaller than the equipment resolution. In both the tomography analysis (Figure 10) and the images in Figure 10, no aligned or coalesced pores are observed, which are known to act as stress concentrators and potential regions for crack nucleation, consequently reducing toughness [30].

The two heat-treatment temperatures did not reduce the porosity concentration; they caused only microstructural changes, as discussed in the microstructural analysis.

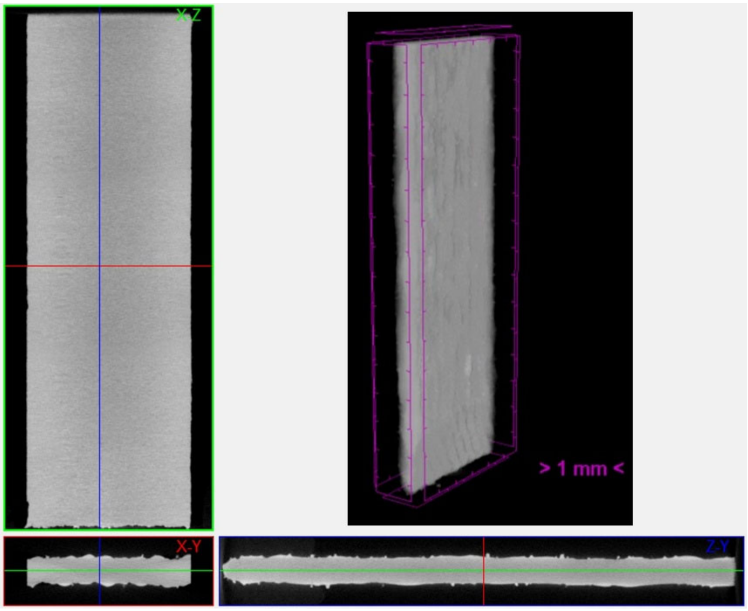

Figure 10. Tomography images of the as-processed sample showing the front, top, and side views, as well as the isometric view.

3.5. X-Ray Diffractometry

Figure 11 shows the X-ray diffraction spectra of different regions of the samples. In the graph, the original substrate and deposit were compared with the heat-treated (HT) samples at 260 °C or 593 °C. Because of the curvature and fluorescence of the analyzed samples, the background patterns were not flat.

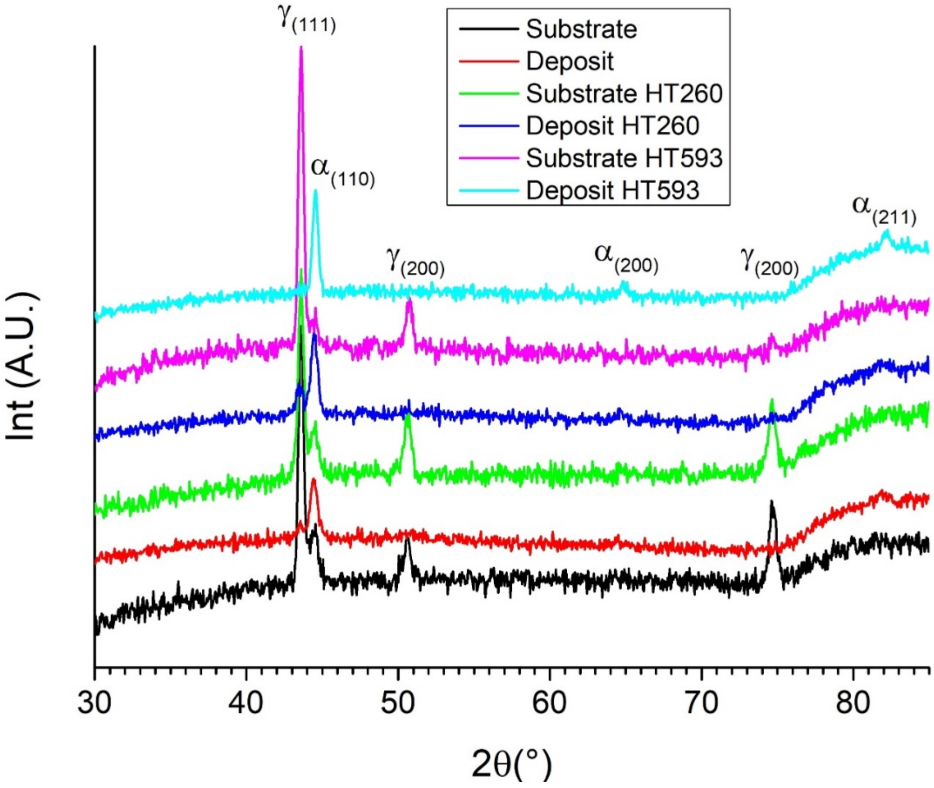

Figure 11. X-ray diffraction patterns of different samples.

According to the relative intensity ratio of the XRD analyses, the percentages of the minor phases in each region were as follows: 14% ferrite substrate, 8% austenite, substrate HT260 17% ferrite substrate HT260, 24% austenite, substrate HT593 8% ferrite, and deposit HT593 full ferrite. These results corroborate the EBSD estimations of phase percentages.

Scheuer et al. [38] studied XRD of wrought AISI 420 steel bars after heat treatment in the range 950 °C and 1050 °C which could be interesting to the current case where austenitizing could occur during the deposition of superposed coats. The authors found some martensite peaks after austenitizing and quenching, particularly near the ferrite α (110) peak (Figure 11). In the current study, the martensite peaks were not verified in either the as-produced or heat-treated deposits, although some retained austenite was verified in deposit HT260. Therefore, as a result of the sequential solidification steps in DED-AM, austenite-stabilizing elements are segregated into interdendritic spaces, which differs from the conventional casting of steel. Heat treatment at 260 °C austenitizes the C- and Ni-rich interdendritic residues.

3.6. Nanoindentation

The nanoindentation test was performed with a capacity to operate in two modules (with a maximum load of 40 mN for the first module and 500 mN for the second module). The load used was 5 mN, and the loading and unloading times were 30 s and 90 s, respectively. Two matrices were created, each with two lines and forty-two indentations. In Figure 12, the nanoindentation map is presented for the samples without heat treatment and those subjected to heat treatment at 260 and 593 °C. The hardness map covered the regions of the substrate, interface, and deposition. For the sample without heat treatment (BM), the average hardness values of the substrate, interface, and deposition were 6.0 GPa, 7.5, and 10 GPa, respectively. In the sample treated at 260 °C, the average hardness values in the substrate, interface, and deposition are 7.0 GPa, 9.0 GPa, and 11 GPa, respectively. In the sample treated at 593 °C, the average hardness was 8.0 GPa. As observed, the heat treatment at 593 °C was more efficient because tempering promoted the homogenization of hardness values, which aimed to reduce its brittleness and improve the toughness of the material. With the heating of the material, the crystalline structure of the material is allowed to relax and rearrange, reducing excessive hardness and increasing toughness, particularly in regions close to the interface.

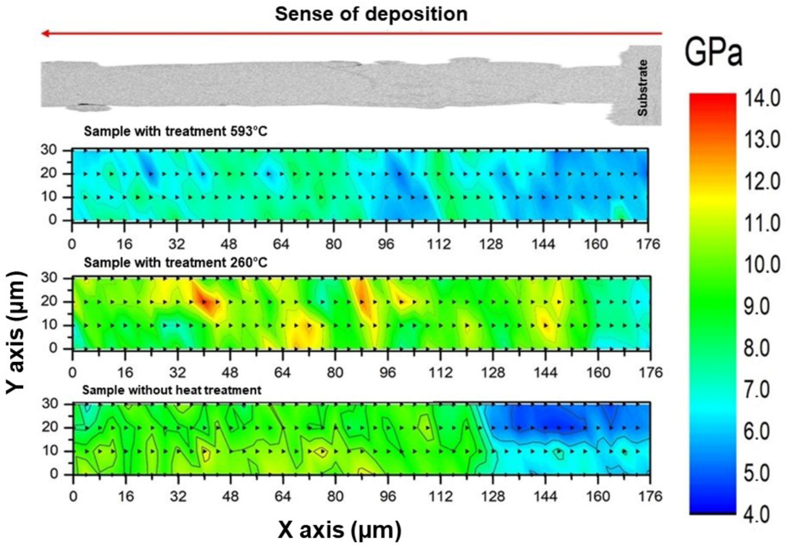

Figure 12. Nanoindentation maps for samples without heat treatment and subjected to heat treatment at 260 °C and 593 °C.

Two loads were used in the ultramicrohardness test, 50 and 100 mN. For the 50 mN load, the spacing between indentations was 0.1 mm, whereas for the 100 mN load, the spacing was 0.2 mm. A total of 36 indentations were made with a 100 mN load, and 20 indentations with a 50 mN load, starting from the substrate and ending at the deposition layer. The ultramicrohardness test results allowed determination of the modulus of elasticity (E). Figure 13 shows the loading curves for 50 and 100 mN loads from the ultramicrohardness tests. In addition, the modulus of elasticity values for the two loads were presented, but only for the sample without heat treatment. The loading curves indicate that after reaching the test loads of 50 mN and 100 mN, the load was maintained for a period before being released. Upon release, the material exhibited elastic recovery, but plastic deformation remained, indicating that the indenter did not return to its initial position (hysteresis). Ultramicrohardness tests were not conducted on the heat-treated samples because the heat treatment did not alter the modulus of elasticity. This property is determined by the crystalline structure of the material as well as the strength of its interatomic bonds [39]. The average values of the modulus of elasticity obtained were (231 ± 18) GPa for the 50 mN load and (224 ± 31) GPa for the 100 mN load. According to the literature, AISI 431 L stainless steel has a modulus of elasticity of 200 GPa [39]. These results indicate that the additive manufacturing process does not significantly alter the modulus of elasticity, as expected, because AM is capable of producing parts with mechanical properties comparable to traditional methods, maintaining a relatively stable modulus of elasticity [39].

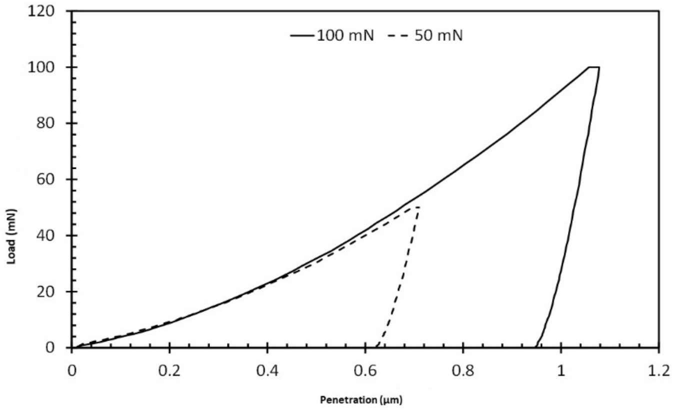

Figure 13. Loading curves of the ultramicrohardness test for loads of 50 and 100 mN for a sample without heat treatment.

3.7. Residual Stresses

Table 3 summarizes the residual stress measurements obtained at the middle (position 1), between the middle and top coats (position 2), and near the last coat (position 3) of the deposit, according to the blade geometry given in the first column. The standard deviation varied at each position between 20 and 55 MPa, although all measurements yielded negative values. Disregarding the blade type, the average residual stress varied from −108 to −176 MPa which is consistent with the literature. Saboori et al. [40] indicated a large residual stress variation in DED AISI 316 L cubes depending on the measurement position, although these authors found residual stress values from −40 and −204 MPa in positions similar to the present study. Kuraman et al. [41] also found highly compressive residual stresses in AISI 316L stringers, exceeding the tensile strength of the hot rolled austenitic stainless steel, i.e., −822 MPa. According to Vyatskikh et al. [42], the buildup of residual stress is material-dependent and can be mitigated by fine-tuning the process parameters and post-AM heat treatment. Unfortunately, the residual stress evaluation of the current deposit alloy has not been reported in the literature.

Table 3. Residual stress measurements for different blade geometries. Unit MPa.

Type	Pos. 1	Pos. 2	Pos. 3	Average	StDev
Supersonic	−68	−98	−158	−108	46
Later	−209	−95	−113	−139	61
Clark	−109	−129	−179	−139	36
Arc	−120	−242	−110	−157	73
Laminar	−210	−168	−151	−176	30

The average residual stress values presented in Table 3 represent approximately 30% of the yield strength of typical AISI 420 steel [43] and are independent of blade type. The predominance of compressive residual stresses in DED-AM steel stringers was also reported by Lu et al. [44] because the mechanical constraints induced by the substrate were gradually reduced, allowing for the free thermal expansion/contraction of the deposited materials.

As the residual stress values did not change appreciably in the different blade types, they were chosen to determine the effect of heat treatment at the two chosen temperatures for the super type blade. The effect of heat treatment was the same, and the measured residual stresses were nullified. The average residual stresses after HT at 260 °C and 593 °C were 1 ± 98 MPa and −1 ± 8 MPa, respectively. The wide variation in the values for the HT 260 °C sample is due to the misfit of the diffraction angle versus the φ angle. One hypothesis is that it is due to the stress relief of some grains, mainly near the open surfaces, and the partial relief of the grains inside the deposit because of the relatively low temperature and time.

3.8. Roughness

In Table 4, the average roughness values of the absolute height variations in the profile (Ra) and the maximum roughness height, referring to the largest difference between a peak and a valley (Rz), are presented for the five studied blades. Because all five blades were produced using the same process parameters, it was possible to calculate the average values for Ra and Rz, which were 24 ± 3 µm and 278 ± 27 µm, respectively.

Table 4. Ra and Rz values of the studied blades.

Blade Geometries	Ra (µm)	Rz (µm)
Later	23.3	324.7
Supersonic	24.9	259.9
Arc	28.1	248.6
Laminar	21.8	279.9
Clark	21.8	289.2
Average ± Standard Deviation	24 ± 3	278 ± 27

Surface roughness is an intrinsic characteristic of additive manufacturing processes, and post-processing may be necessary, depending on the application. Surface roughness is related to process parameters such as scanning speed, laser beam power, scanning strategy, and powder granulometry [21]. The heat treatment performed in this study did not alter the roughness values because the temperatures were not sufficiently high to cause surface melting and thus modify the surface roughness.

3.9. Salt Spray Corrosion

The salt spray corrosion test was conducted in accordance with the ASTM D1654/ASTM B 117 standard [14] in a salt spray chamber, for a period of 1080 h, over 45 days, using analytical-grade sodium chloride as the reagent. This test is pertinent because it has been observed that the growth of AISI 431 L steel by AM is particularly interesting for blades in contact with water vapor. In Figure 14a,b, no corrosion regions were observed in the deposited layers, interface, or substrate. This indicates that the deposited layers, interface, and substrate are resistant to NaCl-rich environments; thus, these blades can be used in such environments. Dark spots were observed in the images taken with an optical microscope. Even after cleaning the samples with Scotch-Brite sponges, detergent, distilled water, and an ultrasonic bath with distilled water for 30 min, it was not possible to completely remove the salt accumulation.

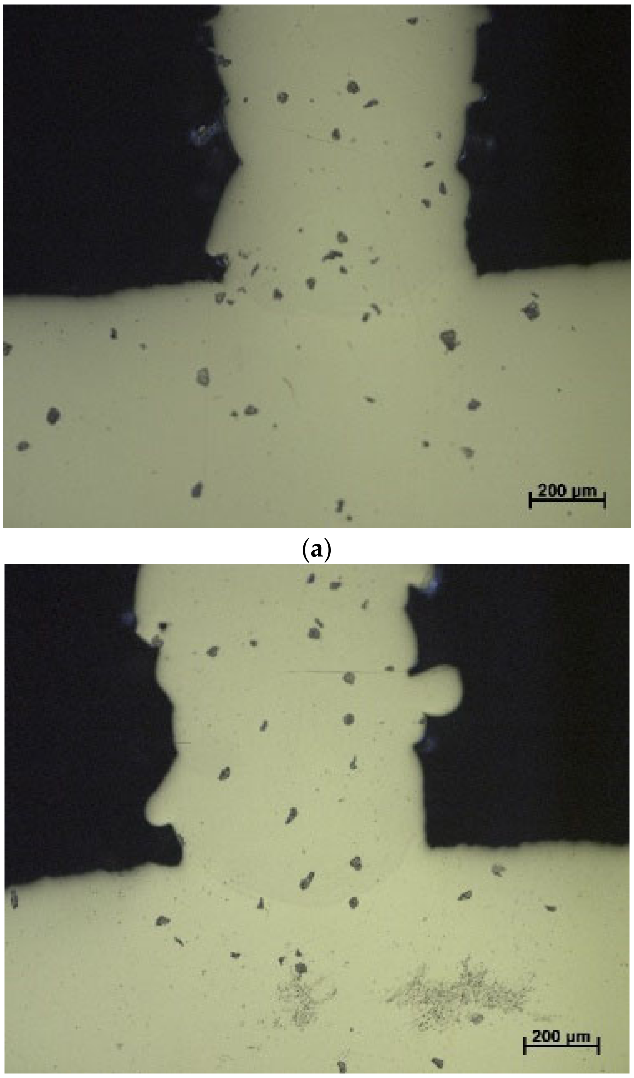

(**a**)

(**b**)

Figure 14. Macrography after salt spray corrosion test: (**a**) arc MO and (**b**) later MO.

In Figure 15a,b, scanning electron microscopy analyses were performed to rule out any oxide formation in the regions of interest. It was observed that there was no oxide formation, but rather an accumulation of NaCl.

It is important to note that the inspection of corrosion damage, usually carried out on the surface of the part and not on its cross-section, is provided for in the standard. However, because of the roughness inherent in the DED process, this direct observation is not applicable.

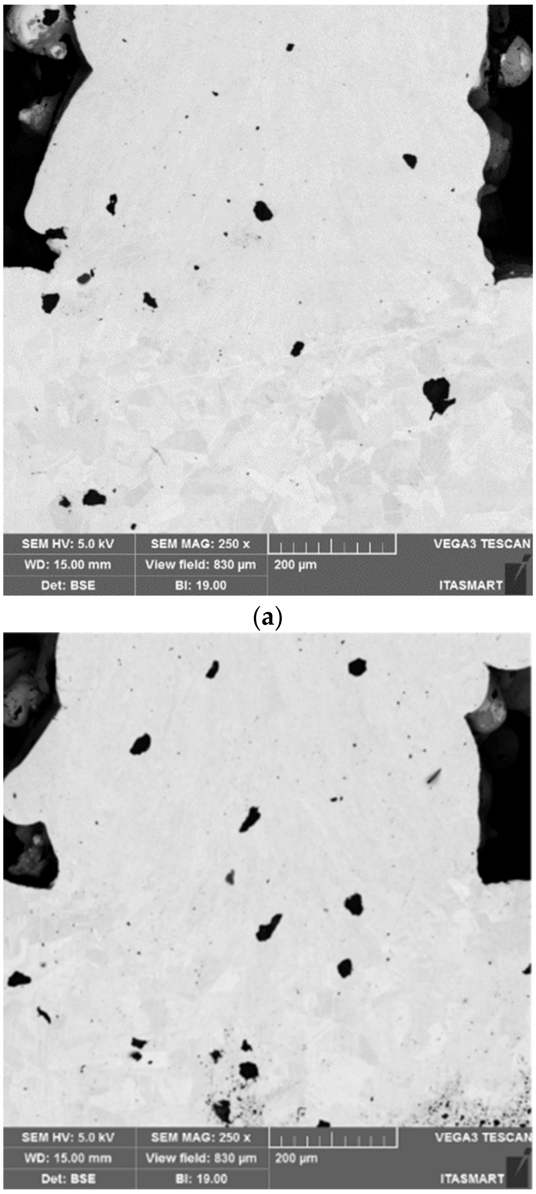

(**a**)

(**b**)

Figure 15. Scanning electron microscope analyses of the samples after corrosion by salt spray: (**a**) arc and (**b**) later.

4. General Discussion

The results obtained in this study demonstrated the feasibility of manufacturing martensitic stainless steel turbine blades using a directed energy deposition (DED) process. The characterization of the fabricated blades provides valuable insights into the microstructural evolution, mechanical properties, and residual stress behavior of AISI 431 L deposited on AISI 304 L stainless steel.

4.1. Comparison with Previous Studies

These findings align with those of previous research on additive manufacturing of stainless steels. The predominantly martensitic microstructure observed in the as-processed condition is consistent with reports by Hemmati et al. [27] and Liu et al. [28], where laser-deposited AISI 431 L exhibited similar characteristics. The presence of interdendritic segregation, also noted in studies on DED of stainless steels [8,9], suggests that the process parameters used in this study were effective in controlling solidification.

4.2. Effect of Processing Parameters

The selection of process parameters is crucial for achieving optimal deposition quality. The relationship between laser power, scanning speed, and powder flow significantly affected the microstructure and porosity. The absence of coalesced pores, as confirmed by tomography, indicated that the selected conditions prevented defect formation, which is a common concern in laser-based additive manufacturing.

4.3. Impact of Heat Treatment

Heat treatment at 260 °C and 593 °C influenced the microstructure and residual stresses of the deposited material. The reduction in grain size at 593 °C suggests that recrystallization occurred, leading to a more homogeneous microstructure. This is in agreement with the findings of previous studies on the tempering of martensitic stainless steels [23,24]. The elimination of residual stresses after heat treatment further supports the effectiveness of post-processing in improving material performance.

4.4. Performance of Different Blade Geometries

The five blade geometries exhibited similar roughness and hardness characteristics, indicating that the process parameters were robust across the different shapes. However, the residual stress measurements showed some variations depending on the location within the blades. Despite these variations, all blades maintained compressive residual stresses, which is beneficial for fatigue resistance in high-performance applications.

4.5. Practical Implications

The successful fabrication of turbine blades using DED suggests that this technique can be employed for both manufacturing and repairing high-value components. The corrosion resistance demonstrated in the salt spray test indicates that the fabricated blades can perform well in aggressive environments such as those encountered in gas turbines. The retention of the mechanical properties after the heat treatment further enhanced the applicability of the DED-fabricated components.

4.6. Future Perspectives

Future research should focus on optimizing the deposition strategies to further refine the microstructure and mechanical properties of fabricated components. Investigating alternative heat treatment cycles and their impact on the phase stability and hardness could provide further insights. Moreover, the application of protective coatings to enhance high-temperature oxidation resistance should be explored. Finally, real-world validation through turbine testing is a crucial step toward the industrial adoption of DED for turbine blade manufacturing.

These findings highlight the potential of DED as a viable method for producing martensitic stainless steel turbine blades, paving the way for further advancements in additive manufacturing for high-performance applications.

5. Conclusions

This study confirmed the feasibility of manufacturing martensitic stainless steel turbine blades using the directed energy deposition (DED) process on an AISI 304 L substrate. The fabricated blades exhibited a predominantly martensitic microstructure, low porosity, and mechanical properties suitable for demanding applications.

Heat treatment at 260 and 593 °C promoted stress relief and recrystallization without significantly affecting the surface roughness or modulus of elasticity. Tomographic analysis verified the absence of critical structural defects, and salt spray tests demonstrated the corrosion resistance, reinforcing the applicability of the material in aggressive environments.

EBSD analyses indicated the absence of crystallographic orientations owing to equiaxial grains before and after heat treatment. Additionally, after heat treatment at 260 °C, the FCC-phase amount increased to 33% compared to approximately 10% of that of the untreated deposit. The heat treatment at 593 °C reduced the FCC phase to approximately 4%. These results were corroborated by the XRD analyses.

As shown by the XRD results, the residual stress values did not change appreciably for the different blade types (108–176 MPa). However, the residual stress value was almost zero after HT at 260 °C and 593 °C, being 1 ± 98 MPa and -1 ± 8 MPa, respectively.

The surface roughness did not change for the five different blades, with average Ra and Rz values of 24 ± 3 μm and 278 ± 27 μm, respectively.

Finally, all the martensitic stainless-steel blades manufactured by directed energy deposition passed the salt spray corrosion test in accordance with the ASTM D1654/ASTM B 117 standards.

The analyzed blade geometries exhibited consistent behavior, with a predominance of compressive residual stresses, suggesting good fatigue resistance. Thus, DED is a promising alternative for manufacturing and repairing turbine blades by combining its structural integrity and favorable mechanical properties. For industrial applications, further research is recommended to investigate fatigue and long-term performance, along with optimization of deposition parameters and heat treatment temperatures. Additionally, exploring the use of protective coatings could enhance oxidation resistance at high temperatures. In summary, the DED process has proven to be an effective approach for producing martensitic stainless steel turbine blades, contributing to advancements in additive manufacturing for engineering applications.

Author Contributions: Conceptualization, M.S.F.d.L.; methodology, C.C.d.A.F., R.H.M.d.S. and F.E.M.; software, R.H.M.d.S. and F.E.M.; validation, R.T.C., D.C. and M.S.F.d.L.; formal analysis, C.C.d.A.F., R.H.M.d.S. and J.G.N.; investigation, C.C.d.A.F.; resources, C.C.d.A.F. and D.C.; data curation, C.C.d.A.F. and J.G.N.; writing—original draft, J.G.N., D.C. and M.S.F.d.L.; writing—review and editing, D.C. and M.S.F.d.L.; supervision, R.T.C., D.C. and M.S.F.d.L.; project administration, M.S.F.d.L.; funding acquisition, R.T.C., D.C. and M.S.F.d.L. All authors have read and agreed to the published version of the manuscript.

Funding: Three (C.C.d.A.F., R.H.M.d.S., and M.S.F.d.L.) authors acknowledge the scientific support and collaboration from Ana Sofia Ramos and Patrícia Freitas Rodrigues from Coimbra University, Portugal, and Diego Javier Celentano and Magdalena Marta Walczak from Pontifical Catholic University of Chile. The authors acknowledge the financial support from the São Paulo Research Foundation (FAPESP), Brazil, Processes #2023/06827-6, and 2016/11309-0. This study was financed in part by the Coordenação de Aperfeiçoamento de Pessoal de Nível Superior, Brazil (CAPES) (Finance Code 001). DLC also thanks the Natural Sciences and Engineering Research Council of Canada (NSERC) for their financial support.

Data Availability Statement: The original contributions presented in this study are included in the article. Further inquiries can be directed to the corresponding author.

Conflicts of Interest: The authors declare no conflict of interest.

References

1. Badiru, A.B. Comprehensive project management of high-end additive manufacturing equipment. In *Additive Manufacturing Handbook*; CRC Press: Boca Raton, FL, USA, 2018; pp. 37–48.
2. Kumar, S.A.; Prasad, R.V.S. Basic principles of additive manufacturing: Different additive manufacturing technologies. In *Additive Manufacturing*; Elsevier: Amsterdam, The Netherlands, 2021; pp. 17–35.

3. Saboori, A.; Aversa, A.; Marchese, G.; Biamino, S.; Lombardi, M.; Fino, P. Application of directed energy deposition-based additive manufacturing in repair. *Appl. Sci.* **2019**, *9*, 3316. [CrossRef]
4. Blaha, R.; Hajnys, J.; Mesicek, J.; Mechali, A.; Krisak, D.; Pagac, M. Review of Directed Energy Deposition (DED) in Component Repair. In *International conference on From Smart City to Smart Factory for Sustainable Future*; Springer Nature: Cham, Switzerland, 2024; pp. 197–205.
5. Tarancón, A.; Esposito, V. *3D Printing for Energy Applications*; John Wiley & Sons: Hoboken, NJ, USA, 2021.
6. Padture, N.P.; Gell, M.; Jordan, E.H. Thermal Barrier Coatings for Gas-Turbine Engine Applications. *Science* **2002**, *296*, 280–284. [CrossRef] [PubMed]
7. Singh, A. *Production, Fabrication, Selection of Stainless Steel*; Dolphin Books: New Delhi, India, 1991.
8. Lu, Z.L.; Li, D.C.; Tong, Z.Q.; Lu, Q.P.; Traore, M.M.; Zhang, A.F.; Lu, B.H. Investigation into the direct laser forming process of steam turbine blade. *Opt. Lasers Eng.* **2011**, *49*, 1101–1110. [CrossRef]
9. Lu, Z.L.; Zhang, A.F.; Tong, Z.Q.; Yang, X.H.; Li, D.C.; Lu, B.H. Fabricating the steam turbine blade by direct laser forming. *Mater. Manuf. Process.* **2011**, *26*, 879–885. [CrossRef]
10. Lucacci, G. Steels and alloys for turbine blades in ultra-supercritical power plants. In *Materials for Ultra-Supercritical and Advanced Ultra-Supercritical Power Plants*; Woodhead Publishing: New Delhi, Delhi, 2017; pp. 175–196.
11. Özdemir, N. Investigation of the mechanical properties of friction-welded joints between AISI 304L and AISI 4340 steel as a function rotational speed. *Mater. Lett.* **2005**, *59*, 2504–2509. [CrossRef]
12. Sabri, K.; Si-Chaib, M.O.; Gaceb, M. Effect of Rejuvenation Heat Treatment on the Degraded Turbine Blades. *J. Fail. Anal. Prev.* **2021**, *21*, 74–82. [CrossRef]
13. *ASTM E407-99*; Standard Practice for Microetching Metals and Alloys. American Society for Testing and Materials: West Conshohocken, PA, USA, 2017. Available online: https://www.astm.org/e0407-99.html (accessed on 12 May 2025).
14. *ASTM D1654*; Standard Test Method for Evaluation of Painted or Coated Specimens Subjected to Corrosive Environments. American Society for Testing and Materials: West Conshohocken, PA, USA, 2024. Available online: https://store.astm.org/d1654-08r16e01.html (accessed on 12 May 2025).
15. Boulila, A.; Boujelbene, M.; Fekiri, C.; Hammami, A. Optimization of manufacturing complex-shaped gas turbine blades. *Measurement* **2019**, *135*, 768–781. [CrossRef]
16. Vdovin, R.A.; Smelov, V.G.; Sufiiarov, V.S.; Borisov, E.V. Designing of the digital casting process for the gas turbine engine blades with a single-crystal structure. In *IOP Conference Series: Materials Science and Engineering*; Institute of Physics Publishing: Bristol, UK, 2018; Volume 441.
17. Bansod, A.V.; Patil, A.P.; Verma, J.; Shukla, S. Microstructure, mechanical and electrochemical evaluation of dissimilar low Ni SS and 304 SS using different filler materials. *Mater. Res.* **2019**, *22*, e20170203. [CrossRef]
18. Akinlabi, E.T.; Mahamood, R.M.; Akinlabi, S.A. Advanced Manufacturing Techniques Using Laser Material Processing. In *Advances in Civil and Industrial Engineering*; IGI Global: Hershey, PA, USA, 2016.
19. Senthilkumaran, K.; Pandey, P.M.; Rao, P.V.M. Influence of building strategies on the accuracy of parts in selective laser sintering. *Mater. Des.* **2009**, *30*, 2946–2954. [CrossRef]
20. Dauntless Flight School, Airfoil Design. Available online: http://faatest.com/books/flt/chapter17/airfoildesign.htm (accessed on 12 May 2025).
21. Sames, W.J.; List, F.A.; Pannala, S.; Dehoff, R.R.; Babu, S.S. The metallurgy and processing science of metal additive manufacturing. *Int. Mater. Rev.* **2016**, *61*, 315–360. [CrossRef]
22. Lashgari, H.R.; Kong, C.; Adabifiroozjaei, E.; Li, S. Microstructure, post thermal treatment response, and tribological properties of 3D printed 17-4 PH stainless steel. *Wear* **2020**, *456–457*, 203367. [CrossRef]
23. Xu, N.; Shen, J.; Zhou, J.; Hu, S. Microstructure and Pitting Corrosion Resistance of AISI 430 Ferritic Stainless Steel Joints Fabricated by Ultrasonic Vibration Assisted Cold Metal Transfer Technique. *Metals* **2022**, *12*, 382. [CrossRef]
24. Porter, D.A.; Easterling, K.E.; Sherif, M.Y. *Phase Transformations in Metals and Alloys*; CRC Press: Boca Raton, FL, USA, 2021.
25. Khoshnaw, F. (Ed.) *Welding of Metallic Materials Methods, Metallurgy, and Performance*; Elsevier: Amsterdam, The Netherlands, 2023.
26. *ASTM E407-99*; Standard Practice for Microetching Metals and Alloys. ASTM International: West Conshohocken, PA, USA, 1999.
27. Hemmati, I.; Ocelík, V.; De Hosson, J.T.M. Microstructural characterization of AISI 431 martensitic stainless steel laser-deposited coatings. *J. Mater. Sci.* **2011**, *46*, 3405–3414. [CrossRef]
28. Liu, Y.; Li, A.; Cheng, X.; Zhang, S.Q.; Wang, H.M. Effects of heat treatment on microstructure and tensile properties of laser melting deposited AISI 431 martensitic stainless steel. *Mater. Sci. Eng. A* **2016**, *666*, 27–33. [CrossRef]
29. Yin, Y.; Tan, Q.; Bermingham, M.; Mo, N.; Zhang, J.; Zhang, M.X. Laser additive manufacturing of steels. *Int. Mater. Rev.* **2022**, *67*, 487–573. [CrossRef]
30. Dowling, N.E.; Kampe, S.L.; Vanlandingham Kral, M. *Mechanical Behavior of Materials: Engineering Methods for Deformation, Fracture, and Fatigue*; John Wiley & Sons: Hoboken, NJ, USA, 2020.

31. Lima, A.S.; Nascimento, A.M.; Abreu, H.F.G.; De Lima-Neto, P. Sensitization evaluation of the austenitic stainless steel AISI 304L, 316L, 321 and 347. *J. Mater. Sci.* **2005**, *40*, 139–144. [CrossRef]
32. Doerr, C.; Kim, J.Y.; Singh, P.; Wall, J.J.; Jacobs, L.J. Evaluation of sensitization in stainless steel 304 and 304L using nonlinear Rayleigh waves. *NDT E Int.* **2017**, *88*, 17–23. [CrossRef]
33. Fonda, R.W.; Rowenhorst, D.J. Crystallographic Variability in Additive Manufacturing. *IOP Conf. Ser. Mater. Sci. Eng.* **2022**, *1249*, 012007. [CrossRef]
34. Kim, D.-K.; Woo, W.; Kim, E.-Y.; Choi, S.-H. Microstructure and mechanical characteristics of multi-layered materials composed of 316L stainless steel and ferritic steel produced by direct energy deposition. *J. Alloys Compd.* **2019**, *774*, 896–907. [CrossRef]
35. Pouranvari, M.; Marashi, P.; Alizadeh-Sh, M. Welding metallurgy of dissimilar AISI 430/DQSK steels resistance spot welds. *Weld. J.* **2015**, *94*, 203s–210s.
36. Gan, W.; Huang, Z.; Liu, C.; Wang, Y.; Zhang, H.; Ni, H. Effect of Mg treatment on inclusion behaviors in 430 ferritic stainless steel during solidification. *J. Mater. Res. Technol.* **2024**, *28*, 3349–3364. [CrossRef]
37. Margerit, P.; Weisz-Patrault, D.; Ravi-Chandar, K.; Constantinescu, A. Tensile and ductile fracture properties of as-printed 316L stainless steel thin walls obtained by directed energy deposition. *Addit. Manuf.* **2021**, *37*, 101664. [CrossRef]
38. Scheuer, C.J.; Cardoso, R.P.; Mafra, M.; Brunatto, S.F. AISI 420 martensitic stainless steel low-temperature plasma assisted carburizing kinetics. *Surf. Coat Technol.* **2013**, *214*, 30–37. [CrossRef]
39. Samuel, E.I.; Paulose, N.; Nandagopal, M.; Selvi, S.P.; Babu, S.N.; Mannan, S.L. Tensile deformation and work hardening behaviour of aisi 431 martensitic stainless steel at elevated temperatures. *High Temp. Mater. Process.* **2020**, *38*, 916–926. [CrossRef]
40. Saboori, A.; Piscopo, G.; Lai, M.; Salmi, A.; Biamino, S. An investigation on the effect of deposition pattern on the microstructure, mechanical properties and residual stress of 316L produced by Directed Energy Deposition. *Mater. Sci. Eng. A* **2020**, *780*, 139179. [CrossRef]
41. Kumaran, M.; Senthilkumar, V.; Justus Panicke, C.T.; Shishir, R. Investigating the residual stress in additive manufacturing of repair work by directed energy deposition process on SS316L hot rolled steel substrate. *Mater. Today Proc.* **2021**, *47*, 4475–4478. [CrossRef]
42. Vyatskikh, A.L.; Wang, X.; Haley, J.; Zheng, B.; Valdevit, L.; Lavernia, E.J.; Schoenung, J.M. Residual stress mitigation in directed energy deposition. *Mater. Sci. Eng. A* **2023**, *871*, 144845. [CrossRef]
43. Buono, V.T.L.; Gonzalez, B.M.; Andrade, M.S. Strain aging of AISI 430 ferritic stainless steel. *Scr. Mater.* **1997**, *38*, 185–190. [CrossRef]
44. Lu, X.; Chiumenti, M.; Cervera, M.; Li, J.; Lin, X.; Ma, L.; Zhang, G.; Liang, E. Substrate design to minimize residual stresses in Directed Energy Deposition AM processes. *Mater. Des.* **2021**, *202*, 109525. [CrossRef]